Chemical Science

Accepted Manuscript

This article can be cited before page numbers have been issued, to do this please use: H. Barber, S. Borusak, A. W. E. Stewart, H. Tahir, N. Scott, D. Shleheck, M. Lee and S. J. Williams, *Chem. Sci.*, 2026, DOI: 10.1039/D6SC02372J.




ROYAL SOCIETY OF CHEMISTRY

rsc.li/chemical-science

View Article Online
DOI: 10.1039/D6SC02372J



# Chiral recognition of 2,3-dihydroxypropanesulfonate by bacterial transport proteins adapted to distinct ecological niches

Helen Barber,[1,2,3,4] Sabrina Borusak,[6] Adam W. E. Stewart,[3,4] Hamza Tahir,[5] Nichollas E. Scott,[5] David Schleheck,[6]* Mihwa Lee,[3,4]* Spencer J. Williams[3,4]*

1 Manchester Institute of Biotechnology, University of Manchester, 131 Princess Street, Manchester M1 7DN, United Kingdom

2 Department of Chemistry, School of Natural Sciences, Faculty of Science and Engineering, University of Manchester, Oxford Road, Manchester M13 9PL, United Kingdom

3 School of Chemistry, University of Melbourne, Parkville, Vic 3010, Australia

4 Bio21 Molecular Science and Biotechnology Institute, University of Melbourne, Parkville, Vic 3010, Australia

5 Department of Microbiology and Immunology, University of Melbourne at the Peter Doherty Institute for Infection and Immunity, Melbourne 3000, Australia

6 Department of Biology, University of Konstanz, Germany

Keywords: sulfur cycle, organosulfur, substrate binding proteins, sulfonates, Roseobacter clade

*Abstract*

2,3-Dihydroxypropanesulfonate (DHPS) is an abundant organosulfonate that links sulfosugar catabolism to sulfur mineralization in marine and gut environments. In surface seawater, DHPS occurs as a dilute, mixed *R*/*S* pool, whereas in the anaerobic gut it is produced predominantly as *S*-DHPS through bacterial sulfoglycolysis pathways. Uptake is proposed to occur via tripartite ATP-independent periplasmic (TRAP) transporters that employ periplasmic substrate-binding proteins (HpsK), but the molecular basis of enantiomer recognition has not been defined. Here, we compare HpsK proteins from the marine bacterium *Ruegeria pomeroyi* and the gut anaerobe

View Article Online
DOI: 10.1039/D6SC02372J



*Bilophila wadsworthia* using proteomics, biophysical analysis, X-ray crystallography, and bioinformatics. *Rp*HpsK binds both *R*- and *S*-DHPS with low-nanomolar affinity ($K_D$ 5–9 nM), whereas *Bw*HpsK binds selectively to *S*-DHPS ($K_D$ 530 nM), representing an ~100-fold difference in affinity and strict stereoselectivity. Crystal structures reveal two contrasting strategies for chiral recognition: *Rp*HpsK accommodates both enantiomers through subtle side-chain "toggling" within an otherwise conserved binding pocket, whereas *Bw*HpsK achieves stereoselectivity through a distinct hydrogen-bonding network and a binding site that sterically excludes *R*-DHPS. Sequence similarity and genome neighbourhood analyses place these proteins in separate clusters associated with oxidative (HpsNOP) or glycyl radical enzyme-linked (HpsGH/HpfGH) pathways. These findings show how changes in binding-site architecture tune ligand stereoselectivity and illustrate the adaptation of TRAP-associated substrate binding proteins to distinct ecological and metabolic niches.

## Introduction

Sulfur is an essential element for life, and its global biogeochemical cycling is mediated by a vast array of organosulfur compounds produced and transformed by photosynthetic and heterotrophic microorganisms.[1-2] Among these, the 3-carbon organosulfonate 2,3-dihydroxypropanesulfonate (DHPS) is an abundant and widely distributed organosulfur metabolite, particularly within marine ecosystems,[3] and the human gut.[4-5] DHPS occurs at micromolar concentrations in ocean surface waters and freshwater environments,[6-7] and bacteria capable of DHPS catabolism are found in the marine photic zone,[8] anoxic sediments[9] and the intestinal tracts of animals.[10] In these diverse settings, DHPS links organosulfur production to sulfur biomineralization, functioning either as a carbon and sulfur source for heterotrophic growth or as an electron acceptor in anaerobic respiration. Importantly, DHPS is encountered under strikingly different chemical and stereochemical regimes: in the ocean surface it exists as a dilute, mixed *R*/*S* pool in seawater,[8, 11] whereas in the anaerobic gut it is generated predominantly as *S*-DHPS from sulfosugar catabolism where it likely accumulates locally to substantially higher concentrations, especially in herbivorous diets rich in the sulfolipid sulfoquinovosyl diacylglycerol (SQDG).[12]

DHPS enters the biosphere through at least two distinct biogenic routes. One major source is direct synthesis by marine algae, including diatoms and coccolithophores, via as yet undefined biosynthetic pathway(s).[8, 13-14] In these autotrophs, DHPS functions as an osmolyte and metabolic

View Article Online
DOI: 10.1039/D6SC02372J



overflow product of photosynthetic carbon fixation. Phytoplankton produce both *R*- and *S*-enantiomers, with enantiomeric ratios that vary across species and environmental conditions.[8] Following release into seawater, DHPS accumulates in the dissolved organic matter pool as a mixed-chiral substrate that supports the growth of heterotrophic bacteria such as *Ruegeria pomeroyi* and other members of the Roseobacter and SAR11 lineages.[7, 15] In these organisms, DHPS is oxidized to *R*-sulfolactate and subsequently converted to sulfite and sulfate,[8, 16] regenerating inorganic sulfur while fuelling bacterial energy metabolism (**Figure 1a**).[17] Assimilation of both enantiomers is thought to be facilitated by the two-component racemase HpsO-HpsP[8, 17] or by an alternative stereochemical interconversion pathway.[18] Together, these pathways allow heterotrophic bacteria to exploit algal DHPS as a major growth substrate: in co-culture with the diatom *Thalassiosira pseudonana*, *R. pomeroyi* derives the majority of its bacterial biomass from DHPS.[19]

A second major source of DHPS is as a product of bacterial degradation of sulfoquinovose (SQ),[20-21] a sulfosugar produced in vast quantities by photosynthetic organisms as the headgroup of SQDG (**Figure S1**).[12, 22] Sulfoglycolytic bacteria are found across a wide range of environments,[23] including terrestrial,[4, 24-25] aquatic,[22, 26-27] and host-associated niches.[4-5, 28-29] In the human gut, prominent SQ degraders such as *Escherichia coli* and *Agathobacter rectalis* use sulfoglycolytic Embden-Meyerhof-Parnas[30] and sulfofructose transaldolase[4, 31] pathways, respectively, to generate *S*-DHPS.[5, 32] In the anoxic distal intestine, the anaerobe *Bilophila wadsworthia* exploits this *S*-DHPS as a terminal electron acceptor in dissimilatory respiration, reducing the released sulfite to hydrogen sulfide (**Figure 1b**).[10] In *B. wadsworthia*, DHPS catabolism involves the glycyl radical enzyme (GRE) DHPS sulfo-lyase HpsG, together with its activating protein HpsH, producing hydroxyacetone and sulfite (**Figure S1**).[10] Notably, *B. wadsworthia* quantitatively consumes DHPS produced by sulfoglycolysis by *A. rectalis*, whereas only ~50% of externally supplied racemic DHPS is metabolized.[5] This stereoselective utilisation indicates that *B. wadsworthia* respires exclusively the *S*-enantiomer of DHPS. Consistent with this interpretation, the *B. wadsworthia* genome lacks the *hpsOP* epimerase genes required for interconversion of DHPS enantiomers, supporting a strictly *S*-DHPS specific respiratory pathway. In other gut-associated bacteria, an alternative GRE-dependent pathway involving HpfGH dehydrates DHPS to sulfopropanaldehyde, which can act as an electron sink through reduction by

View Article Online
DOI: 10.1039/D6SC02372J



HpfD[33] to hydroxypropanesulfonate, or can be oxidized by HpfXYZ[10] to produce sulfopropanoate and ATP (**Figure S1**).

In summary, these routes create two contrasting ecological and stereochemical contexts for DHPS utilization. In the marine photic zone, DHPS derives primarily from phytoplankton production and is released into seawater as a dilute mixed *R*/*S* pool, where uptake is expected to be strongly competitive. In contrast, in the anoxic distal gut, DHPS arises predominantly as *S*-DHPS from bacterial sulfoglycolysis of sulfoquinovose and functions as a respiratory electron acceptor for anaerobes such as *B. wadsworthia*, where DHPS supply is expected to be more episodic and locally enriched. These distinct niches predict different selective pressures on transport: a marine system benefiting from high-affinity, enantiomer-flexible acquisition, versus a gut system favoring enantiomer-selective import.

Uptake of DHPS by *R. pomeroyi* and *B. wadsworthia* is proposed to occur via periplasmic-binding protein–dependent transport systems, specifically tripartite ATP-independent periplasmic (TRAP) transporters that employ soluble DHPS-binding proteins. TRAP transporters comprise a periplasmic substrate-binding protein (the P-domain) and two integral membrane subunits (the Q- and M-domains; in some cases fused into a single polypeptide) that together form a secondary active transporter (**Figure 1c**).[34] Upon ligand binding, the substrate-loaded P-domain docks onto the periplasmic face of the membrane complex, coupling conformational changes within the binding protein to translocation through the membrane. Transport is powered by the electrochemical gradient of sodium ions or protons. Recent cryo-EM structures of the sialic acid transporter SiaQM[35-36] and the isethionate transporter IseQM[37] reveal that the M-domain operates via an elevator-type mechanism, in which a mobile transport subdomain carrying the substrate-binding site moves vertically relative to a stationary scaffold, alternately exposing the substrate site to the periplasm and cytoplasm during the transport cycle.[34] Consistent with a role in DHPS uptake, deletion of the DHPS-binding protein HpsK in *R. pomeroyi* impairs growth on DHPS[38] and reduces fitness in co-culture with the DHPS-producing diatom *T. pseudonana*.[19]

Here we study the DHPS-binding proteins (HpsK) from *Ruegeria pomeroyi* and *Bilophila wadsworthia* to define how solute recognition has been tailored to contrasting ecological and stereochemical environments. We show that *R. pomeroyi* HpsK binds both DHPS enantiomers with low-nanomolar affinity, consistent with adaptation to a dilute, mixed-chiral marine pool, whereas *B. wadsworthia* HpsK exhibits strict stereoselectivity for *S*-DHPS, reflecting its origin as

View Article Online
DOI: 10.1039/D6SC02372J



the product of sulfoquinovose sulfoglycolysis. Structural analyses reveal distinct binding-pocket architectures that enable dual versus single enantiomer recognition, demonstrating how evolutionary pressures imposed by environmental availability and metabolic context have shaped substrate specificity.

## Results and Discussion

*Proteomics analysis of Ruegeria pomeroyi grown on DHPS*

To experimentally validate the role of the proposed *R. pomeroyi* DHPS-binding protein HpsK in DHPS metabolism, we performed comparative proteomic analysis of the model strain DSS-3 grown on either *R*-DHPS or *S*-DHPS as sole carbon sources, relative to glucose. Under both DHPS conditions, proteins encoded within the *hpsKLMNOPQR–slcD*, *soeABC–pta–xsc*, and *cuyAZ* loci were significantly increased in abundance (**Figure 2, Supplementary Data 1**). These data support operation of the previously proposed DHPS catabolic pathway in *R. pomeroyi*,[7, 39] involving substrate import via the HpsK-binding protein and TRAP transporter HpsLM, racemisation by the NAD(P)-dependent DHPS-2-oxidoreductases HpsOP, and subsequent oxidation by a DHPS-3-dehydrogenase to generate sulfolactate (SL). The observed induction profile is consistent with prior reports of growth on DHPS enantiomers compared with acetate,[7] confirming that both stereoisomers are metabolized through the same core pathway.

The downstream fate of SL in *R. pomeroyi* remains unresolved but is proposed to proceed via oxidation to sulfopyruvate, followed by transamination to cysteate and cleavage by the CuyA sulfolyase to yield pyruvate, ammonium, and sulfite.[7] Alternatively, sulfopyruvate may undergo decarboxylation to sulfoacetaldehyde, which can then be cleaved by the thiamine diphosphate–dependent enzyme Xsc to generate acetyl phosphate and sulfite.[7] The elevated abundance of CuyA during growth on both *R*- and *S*-DHPS supports preferential flux through the cysteate-dependent branch. HpsR is the likely transcriptional regulator governing the early steps of DHPS degradation involving HpsNOP. Consistent with sulfite production from a sulfolyase reaction, SoeA was also enriched under DHPS growth conditions. SoeA forms part of the SoeABC sulfite dehydrogenase complex, which oxidizes sulfite to sulfate for detoxification and export while transferring electrons to coenzyme Q, thereby supporting ATP generation via oxidative phosphorylation.[40-41]

One notable proteomic distinction between growth on *R*-DHPS and *S*-DHPS was the increased abundance of SPO0660 only under *S*-DHPS condition (**Figure S2**). This protein is

View Article Online
DOI: 10.1039/D6SC02372J



annotated as an *N*-acetyltaurine-binding protein (NaaA), and its gene resides within a cluster encoding an ABC transporter and an *N*-acetyltaurine amidohydrolase (NaaS), based on functional characterization in *Cupriavidus necator*.[42] The role of these homologous proteins in *R. pomeroyi* was not investigated further in the present study.

*RpHpsK binds both DHPS enantiomers with low nanomolar affinities*

We first evaluated binding of the DHPS enantiomers to *Rp*HpsK (heterologously expressed in *Escherichia coli*) using nanoscale differential scanning fluorimetry (nanoDSF). Addition of either *R*- or *S*-DHPS (2 mM) to recombinantly expressed and purified *Rp*HpsK produced marked thermal stabilization, with identical increases in melting temperature (ΔTm) of 15.7 K for each enantiomer, relative to the ligand-free protein (**Figure 3a** and **Table S1**). These large and equivalent shifts indicate that *Rp*HpsK binds both enantiomers with high affinity under saturating conditions. To assess substrate selectivity, we examined binding of structurally-related organosulfonates likely to be encountered by *R. pomeroyi*, including sulfolactate, cysteinolate, isethionate, sulfopropanoate, hydroxypropanoate and sulfoquinovose (**Table S1**), which showed *Rp*HpsK displayed a clear preference for DHPS. The closest analogue, 3-hydroxypropanesulfonate (HPS), induced a ΔTm of 9.9 K, whereas isethionate (2-hydroxyethanesulfonate) and sulfolactaldehyde produced more modest increases of 3.4 K and 6.0 K, respectively; the remaining compounds caused only minor stabilization (**Table S1**).

To quantify ligand binding, we employed isothermal titration calorimetry (ITC). Initial titrations with DHPS indicated exceptionally tight binding, with dissociation constants in the low-nanomolar range. Under these conditions, direct ITC yielded a near-stoichiometric, vertical isotherm, precluding reliable determination of $K_D$ values. In contrast, the DHPS analogues HPS and isethionate, both of which gave intermediate ΔTm shifts in nanoDSF experiments, displayed affinities within the measurable range. HPS bound with a $K_D$ value of 0.92 μM (ΔH = −14.8 kcal mol$^{-1}$, and ΔS = −22 cal mol$^{-1}$ K$^{-1}$), whereas isethionate bound more weakly, with a $K_D$ value of 62.4 μM (ΔH = −10.0 kcal mol$^{-1}$, and ΔS = −14 cal mol$^{-1}$ K$^{-1}$) (**Figure S3**, **Table S2**). Assuming a conserved binding pose relative to DHPS, comparison of these truncated analogues provides insight into contributions of the hydroxyl groups to affinity. HPS lacks the C2-hydroxyl group, whereas isethionate lacks the C3-hydroxymethyl substituent. The substantially weaker binding of isethionate suggests that interactions involving the C3 position contribute more strongly to affinity

View Article Online
DOI: 10.1039/D6SC02372J



than those at C2. This interpretation should be treated cautiously; the shorter two-carbon backbone of isethionate likely reduces hydrophobic and van der Waals contacts within the binding pocket in addition to removing a hydroxyl group that may be involved in hydrogen-bonding interactions.

To accurately quantify DHPS binding, we employed a ligand-displacement ITC strategy, using a weakly binding reference ligand to distribute the heat signal across injections and thereby resolve these high-affinity interactions.[43] HPS ($K_D$ = 0.92 μM) was used as the competing ligand. Under these conditions, *R*-DHPS bound *Rp*HpsK with $K_D$ = 5.1 nM (ΔH = −19.6 kcal mol$^{-1}$, and ΔS = −28 cal mol$^{-1}$ K$^{-1}$), while *S*-DHPS bound with $K_D$ = 9.2 nM (ΔH = −20.4 kcal mol$^{-1}$, and ΔS = −31 cal mol$^{-1}$ K$^{-1}$) (**Figure 3b**, **Figure S4** and **Table S2**). Comparison with HPS reveals that incorporation of the C2-hydroxyl group in DHPS enhances affinity by approximately two orders of magnitude. Thus, while truncation at C3 (as in isethionate) substantially weakens binding, the presence of both hydroxyl substituents in DHPS enables exceptionally tight, enthalpically driven association. The near-equivalent thermodynamic signatures for *R*- and *S*-DHPS indicate that *Rp*HpsK accommodates both stereoisomers with minimal energetic penalty, and with an enthalpic cost, consistent with large domain closure occurring upon ligand binding (vide infra).

The nearly identical binding affinities measured for *R*- and *S*-DHPS indicate that *Rp*HpsK accommodates both enantiomers within a single substrate-binding pocket, with comparable binding constants and closely matched enthalpic and entropic contributions. Dual recognition of opposite stereoisomers by a single solute-binding protein is uncommon but not unprecedented. Examples include ABC transporter–associated SBPs that bind both D- and L-cysteine (*Escherichia coli* FliY),[44] D- and L-methionine (*Neisseria meningitides* MetQ),[45] and a TRAP/TTT-associated SBP that binds D- and L-malate (*Rhodopseudomonas palustris* MatC).[46] Notably, only MatC exhibits affinities for both enantiomers within the same order of magnitude, as observed here for *R*- and *S*-DHPS.

*X-ray crystallography defines recognition of DHPS enantiomers by RpHpsK*

To elucidate the structural basis for dual enantiomer recognition by *Rp*HpsK, we determined crystal structures of the apo protein and of complexes with *R*- and *S*-DHPS. As observed for other solute-binding proteins, apo-*Rp*HpsK adopts an open conformation featuring an accessible substrate-binding cleft. Structures solved in two space groups (*P*1 and $P2_1$; **Table S3**) at 1.47 and 1.90 Å resolution, respectively, revealed similar open states (**Figure 4** and **Figure S5a**). Upon

View Article Online
DOI: 10.1039/D6SC02372J



ligand binding, *Rp*HpsK undergoes a pronounced conformational transition to a closed state, in which the two globular domains converge through a hinge-like "Venus flytrap" motion centred on a bending helix (**Figure 4** and **Figure S5b**). This domain closure, corresponding to a 23.8° rotation, encapsulates the ligand and seals the binding pocket. The resulting electron density is well defined, permitting unambiguous assignment of DHPS stereochemistry in complexes with *R*- and *S*-DHPS, refined to 1.96 and 1.65 Å resolution, respectively (**Figure 4b** and **Figure S6**).

The overall architecture of the ligand-binding site in *Rp*HpsK is essentially unchanged despite the opposite stereochemistry of the two DHPS enantiomers (**Figure 4b, c**). The positions of the carbon backbone, sulfonate group, and 3-hydroxyl substituent are highly similar in the *R*- and *S*-DHPS complexes, falling within the estimated coordinate errors derived from maximum-likelihood refinement (0.13 Å and 0.08 Å for the *R*- and *S*-DHPS complexes, respectively). The largest positional difference is observed at C1, with a displacement of 0.34 Å. In both structures, the sulfonate group is anchored by a conserved hydrogen-bonding network involving Arg184, Arg207, Asn128, and Ser125, while the 3-hydroxyl group engages Tyr75 and Asp272. Coordination of the 2-hydroxyl group is achieved through a subtle rearrangement of side-chain interactions. In the *S*-DHPS complex, the 2-hydroxyl group forms hydrogen bonds with Gln274 and Asp272. Asp272, which also coordinates the 3-hydroxyl group in both complexes, adopts a geometry that permits nearly identical hydrogen-bond distances to the 2-hydroxyl of *R*- and *S*-DHPS (2.6–2.7 Å). In the *R*-DHPS complex, a small shift in Gln274 reorients its interaction toward the 3-hydroxyl group, with Arg184 assuming coordination of the 2-hydroxyl group. Thus, dual enantiomer recognition is achieved through conservation of the overall binding pose and most hydrogen-bonding interactions, coupled with a minimal "toggling" of side-chain contacts at the 2-hydroxyl position that accommodates inversion of stereochemistry without perturbing the binding pocket architecture.

To assess the contribution of residues implicated in DHPS binding, we generated three *Rp*HpsK site-directed mutants: R184A, D272A and Q274A. NanoDSF analysis showed that the R184A and D272A substitutions caused substantial reductions in melting temperature, and neither mutant was stabilized by either *R*- or *S*-DHPS (**Figure S7, Table S4**). These substitutions therefore appear to have broader effects on protein stability, limiting interpretation of their effects on ligand binding. In contrast, the Q274A mutant retained a melting temperature comparable to that of wild-type *Rp*HpsK and was stabilized by both DHPS enantiomers. Whereas *R*- and *S*-DHPS each

View Article Online
DOI: 10.1039/D6SC02372J



increased the melting temperature of wild-type *Rp*HpsK by 15.7 K, the corresponding increases for Q274A were reduced to 12.3 K with *R*-DHPS and 10.9 K with *S*-DHPS. Consistent with this reduced ligand-induced stabilization, ITC analysis showed that the Q274A substitution weakened binding of both DHPS enantiomers, with a stronger effect on *S*-DHPS (**Figure S7**, **Table S5**). The affinity for *R*-DHPS decreased approximately 30-fold to $K_D$ = 150 nM, whereas the affinity for *S*-DHPS decreased approximately 170-fold to $K_D$ = 1,600 nM. These data support a role for Gln274 in DHPS recognition, consistent with the proposed toggling interaction in which this residue hydrogen bonds to the 3-hydroxyl group of *R*-DHPS and the 2-hydroxyl group of *S*-DHPS.

*Proteomics analysis of Bilophila wadsworthia grown on DHPS*

Unlike *R. pomeroyi*, *Bilophila wadsworthia* cannot utilize DHPS as a sole carbon source; instead, DHPS functions as a terminal electron acceptor to support anaerobic respiration.[5] To examine the molecular basis of DHPS respiration, *B. wadsworthia* 3.1.6 was grown with either racemic DHPS or sulfite as electron acceptors, and with L-lactate as electron donor and carbon source, and the resulting proteomes were compared. As discussed in the introduction, under these conditions only *S*-DHPS will be consumed.[5] Proteins significantly increased in abundance under DHPS-respiring conditions included HpsG, HpsH, and HpsK, encoded within the *hpsGHKLM* locus (**Figure 5, Supplementary Data 2**).

HpsGH comprise a two-component glycyl radical enzyme (GRE) system, consisting of the radical SAM activating enzyme HpsH and its catalytic partner HpsG, an *S*-DHPS sulfolyase.[10] HpsG catalyzes C–S bond cleavage of *S*-DHPS to yield sulfite and hydroxyacetone; the liberated sulfite is subsequently reduced to $H_2S$ during anaerobic respiration by the cytosolic DsrABC proteins[47-48] and the DsrMKJOP transmembrane complex,[49] with the reduction being driven by lactate as electron donor. Hydroxyacetone is not utilized further. The proteomic enrichment of HpsK and HpsL further supports their assignment as components of a TRAP-type transporter, with HpsK functioning as the DHPS substrate-binding protein. Based on genomic context, Liu and co-workers identified *Bw*HpsK and demonstrated binding of racemic DHPS, but did not assess enantiomer discrimination.[10] In the same study, the crystal structure of sulfo-lyase HpsG was obtained in complex with *S*-DHPS following soaking with racemic DHPS, implying stereoselective catalysis by HpsG. Together, these observations raise the question of how *B. wadsworthia* discriminates between the two DHPS enantiomers *in vivo*. In addition to the proteins

View Article Online
DOI: 10.1039/D6SC02372J



from the *hpsGHKLM* locus, three other putative substrate-binding proteins were enriched under DHPS growth conditions: HMPREF0179_00063 and HMPREF0179_00064 (annotated as associated with TRAP transporters) and HMPREF0179_02569 (annotated as associated with an ABC transporter). These proteins were not functionally characterized further but were investigated through bioinformatics analysis (*vide infra*).

*BwHpsK selectively binds S-DHPS*

To define the stereochemical specificity of *Bw*HpsK (heterologously expressed in *E. coli*), we first examined ligand-induced thermal stabilization using nanoDSF. Addition of *S*-DHPS (2 mM) to recombinantly expressed and purified *Bw*HpsK resulted in pronounced stabilization, with a ΔTm of +13.7 K relative to the apo protein. In contrast, *R*-DHPS produced only a minimal shift (ΔTm of +1.5 K), indicating strong stereoselective preference for *S*-DHPS (**Figure 6a**). Consistent with this selectivity, *Bw*HpsK displayed narrow substrate tolerance when tested against structurally related organosulfonates. Aside from *S*-DHPS, the largest thermal shift was observed for sulfoacetaldehyde (ΔTm = +6.4 K), whereas all other ligands induced ΔTm values below 3 K, underscoring the high specificity of the binding pocket.

Quantitative analysis by ITC confirmed selective high-affinity binding of *S*-DHPS, yielding a $K_D$ value of 530 nM (ΔH = −8.6 kcal mol$^{-1}$ and ΔS = 0.15 cal mol$^{-1}$ K$^{-1}$) (**Figure 6b**, **Figure S8**, and **Table S6**). Under identical conditions, titration with *R*-DHPS produced no measurable heat change, consistent with the absence of detectable binding. Together, these data demonstrate that, in contrast to the enantiomer-permissive *Rp*HpsK, *Bw*HpsK is a stereoselective binding protein tuned specifically to *S*-DHPS.

*X-ray crystallography defines selective recognition of S-DHPS by BwHpsK*

To define the structural basis of stereoselective DHPS recognition, we determined crystal structures of apo-*Bw*HpsK and of *Bw*HpsK in complex with *S*-DHPS. The apo structure reveals conformational heterogeneity, with one protomer adopting a fully open state and the other a partially closed state, differing by a root-mean-square deviation (r.m.s.d.) of 1.48 Å (**Figure 7** and **Figure S9**), suggesting that *Bw*HpsK samples multiple conformations in the absence of ligand. Upon *S*-DHPS binding, the protein adopts a fully closed conformation. As observed for *Rp*HpsK,

View Article Online
DOI: 10.1039/D6SC02372J



ligand binding induces a hinge-like "Venus flytrap" rotation that brings the two domains together and seals the substrate-binding pocket (**Figure 7** and **Figure S9**).

The *Bw*HpsK•*S*-DHPS complex was refined to near-atomic resolution (1.05 Å), enabling unambiguous assignment of ligand stereochemistry. The binding pocket reveals an extensive network of hydrogen-bonding and van der Waals interactions that explains selective recognition of *S*-DHPS (**Figure 7b,c** and **Figure S10**). As in *Rp*HpsK, the sulfonate group is anchored by two arginine residues (Arg152 and Arg173) and an asparagine (Asn95), and a conserved tryptophan (Trp196 in *Bw*HpsK; Trp230 in *Rp*HpsK) caps the binding site, providing hydrophobic contacts with the DHPS carbon backbone. However, beyond these conserved sulfonate-binding interactions, the coordination network diverges markedly from that of *Rp*HpsK. In *Bw*HpsK, the 3-hydroxyl group of *S*-DHPS is coordinated by Glu74 and His42, while the 2-hydroxyl group engages Asn213 and Trp238. Consequently, the overall orientation of *S*-DHPS within the *Bw*HpsK binding pocket differs substantially from that observed in the *Rp*HpsK•*S*-DHPS complex (**Figure 7c**), reflecting a distinct architectural solution to substrate recognition.

Although the global folds of *Rp*HpsK and *Bw*HpsK are similar (**Figure S11b**), the proteins share only 20.3% sequence identity (**Figure S11a**), reshaping the pocket geometry. Moreover, the loops that define the ligand-binding cavity adopt markedly different conformations (**Figure S11c**). These differences underpin their contrasting specificities: *Rp*HpsK accommodates both DHPS enantiomers, whereas *Bw*HpsK is stereoselective for *S*-DHPS. Modeling inversion at C2 indicates that an *R*-configured 2-hydroxyl group would disrupt the hydrogen-bonding interaction with Trp238 and introduce an unfavorable steric clash with Trp196, providing a structural basis for exclusion of *R*-DHPS.

*Sequence similarity network analysis of HpsK and related organosulfonate binding proteins*

To place *Rp*HpsK and *Bw*HpsK within the broader landscape of TRAP-associated organosulfonate-binding proteins, we analysed sequence relationships using tools from the Enzyme Function Initiative (EFI).[50-52] Following an approach similar to that of Vetting and co-workers,[53] we constructed a sequence similarity network (SSN) comprising 92,628 TRAP-associated solute-binding protein (SBP) sequences from InterPro family IPR018389. Application of UniRef50 redundancy reduced network complexity to 8,672 nodes. Within this global SSN, *Rp*HpsK and *Bw*HpsK localise to distinct sub-clusters, consistent with their divergent ligand

View Article Online
DOI: 10.1039/D6SC02372J



specificities (**Supplementary Data 3**). Genome neighbourhood analysis within a ±20 gene window using the EFI-GNT webtool identified six clusters associated with either *hpsNOP* (Pfams PF00815, PF13561, PF00107–PF08240) or *hpsGH*/*hpfGH* (Pfams PF01228–PF02901, PF04055) loci. These sequences were expanded from UniRef50 to UniRef IDs and used to construct SSNs at various alignment scores (**Figure S12**). We selected an SSN with alignment score of 80 (~40% sequence identity) that comprises six major clusters and two singleton sequences (**Figure 8**).

TRAP associated proteins HMPREF0179_00063 and HMPREF0179_00064, which were enriched during racemic DHPS growth of *B. wadsworthia* 3.1.6, were not present in the DHPS/isethionate-specific subset SSN. In the full TRAP-associated SSN, they form a small cluster (<10 members) lacking clear genome neighbourhood associations. While these may represent an additional group of DHPS-responsive transporters, current data does not permit functional assignment.

In the refined SSN (**Figure 8a**), clusters are coloured according to genome neighbourhood content. Three biochemically-characterised DHPS-binding proteins localise to clusters 2, 3, and 6. *Rp*HpsK resides in cluster 2, composed predominantly of proteins associated with HpsNOP variant pathways. *Bw*HpsK localises to cluster 6, enriched in HpsGH/HpfGH encoding gene neighbourhoods. Cluster 3 contains the SAR11 *Candidatus* Pelagibacter ubique[15] isethionate and *R*- and *S*-DHPS binding protein SAR11_0864 and is likewise associated with gene clusters encoding HpsNOP-type systems. In contrast, characterised isethionate-binding proteins (IseP) from *Desulfovibrio piger*[54] and *Oleidesulfovibrio alaskensis*[55] fall within cluster 4, whose members are primarily linked to glycyl radical enzyme (GRE) loci corresponding to the isethionate-specific IslAB pathway.[56] Clusters 1 and 5 contain proteins encoded near HpsOP or GRE encoding loci, respectively, but no representatives have yet been biochemically characterised.

A phylogenetic tree constructed from UniRef90 representative sequences (**Figure S13**) reveals that clusters 1, 4, 5 and 6 are more closely related to one another than to clusters 2 and 3, with clusters 2 and 3 representing the most divergent pair. This topology indicates that similar genomic contexts, such as association with *hpsNOP* loci, do not necessarily reflect close evolutionary relationships among the binding proteins. Instead, the phylogeny suggests multiple evolutionary solutions for DHPS recognition, with functional specialisation likely arising

View Article Online
DOI: 10.1039/D6SC02372J



independently in distinct lineages. The close relationship between clusters 4 and 5 is consistent with their shared association with GRE-dependent organosulfonate catabolic pathways.

Phylogenetic colouring of the SSN (**Figure 8b**) reveals ecological partitioning. Cluster 4, containing isethionate binding IseP and associated with GRE-mediated isethionate degradation, is dominated by Bacillati and Thermodesulfobacteriota. Cluster 2, containing *Rp*HpsK, spans diverse Alpha-, Beta-, and Gammaproteobacteria, consistent with HpsNOP-type systems distributed across marine Proteobacteria. Cluster 3, which includes SAR11 proteins and represents *hpsNOP* variant pathways, is likewise composed predominantly of Alpha-, Beta-, and Gammaproteobacteria. Cluster 6, containing *Bw*HpsK, is enriched in Thermodesulfobacteriota and Gammaproteobacteria, lineages commonly associated with anaerobic environments.

Collectively, these analyses indicate that HpsK proteins associated with GRE-dependent pathways (HpsGH/HpfGH/IslAB) are preferentially linked to anaerobic lineages, whereas HpsK proteins coupled to HpsNOP-type oxidative pathways are broadly distributed across Proteobacterial taxa (**Figures 8, 9**). Given that Proteobacteria dominate the epipelagic ocean, this distribution supports a widespread ecological role for HpsNOP-associated DHPS uptake in marine surface waters. Notably, HpsK proteins from different clusters share low sequence identity (<40% between clusters), yet converge on DHPS recognition despite divergent pocket architectures and binding selectivities (**Table S1**), suggesting repeated evolutionary adaptation to an abundant organosulfonate substrate across distinct ecological niches.

## Conclusions

This study reveals how solute-binding proteins have evolved to accommodate sharply contrasting ecological and stereochemical regimes of a globally abundant organosulfonate metabolite. The DHPS-binding protein from the marine bacterium *Ruegeria pomeroyi* binds both *R*- and *S*-DHPS with low-nanomolar affinity ($K_D$ 5–9 nM), approximately 100-fold tighter than the *S*-selective binding observed for *Bilophila wadsworthia* HpsK ($K_D$ 530 nM) (**Figure 10**). This difference in affinity likely reflects adaptation to distinct environmental contexts: a dilute, mixed-chiral DHPS pool in the competitive, high-salinity marine photic zone versus a locally enriched, stereochemically defined *S*-DHPS pool in the anoxic gut. High-resolution crystal structures demonstrate that these functional differences arise from divergent architectural solutions within a conserved solute-binding protein fold. *Rp*HpsK achieves dual enantiomer recognition through

View Article Online
DOI: 10.1039/D6SC02372J



conservation of overall ligand pose combined with side-chain interaction "toggling" at the 2-hydroxyl position, enabling near-identical thermodynamic profiles for both stereoisomers. In contrast, *Bw*HpsK employs a distinct hydrogen-bonding network and reshaped binding loops that enforce strict stereochemical selection, structurally excluding *R*-DHPS through loss of key interactions and steric conflict.

Bioinformatic analysis places these DHPS proteins within discrete sequence clusters linked to distinct metabolic gene neighbourhoods. HpsK proteins associated with HpsNOP oxidative pathways are broadly distributed across Proteobacteria, particularly marine lineages, whereas those linked to GRE-dependent HpsGH/HpfGH systems are enriched in anaerobic taxa. Despite low sequence identity between clusters, these proteins converge on DHPS recognition, highlighting repeated evolutionary adaptation of TRAP-associated binding proteins to a common substrate across diverse ecological niches. Together, these findings demonstrate that environmental concentration and stereochemical composition can impose measurable selective pressures on solute acquisition systems. The comparative analysis of *Rp*HpsK and *Bw*HpsK provides a molecular framework for understanding how substrate-binding proteins evolve to balance affinity, specificity, and metabolic integration within distinct ecological landscapes of the global sulfur cycle.

## Author contributions

S. J. W. and M. L. conceived the project. M. L., H. B., A. W. E. S., S. B., H. T., and N. E. S. performed the investigation. S. J. W. and D. S. supervised the project. M. L., H. B., and S. B. performed formal analysis. S. J. W. and M. L. wrote the original draft of the manuscript. All authors reviewed and edited the manuscript.

## Conflicts of interest

The authors declare that they have no conflicts of interest with the contents of this article.

## Data availability

The mass spectrometry proteomics data has been deposited in the Proteome Xchange Consortium via the PRIDE partner repository[57] with the data set identifier: PXD069364 (for the proteomics

View Article Online
DOI: 10.1039/D6SC02372J



analysis of *Ruegeria pomeroyi* grown on DHPS) and PXD075985 (for the proteomics analysis of *Bilophila wadsworthia* grown on DHPS).

Data is accessible for the reviewer. With PXD069364 accessible with the Username: reviewer_pxd069364@ebi.ac.uk Password: 0neQwMDNCapv and PXD075985 accessible with the Username: & Password: eQqiVnyXzLBp

Structural data (atomic coordinates) of HpsK crystal structures have been deposited with the Protein Data Bank (PDB accession codes: 24GC (apo-*Rp*HpsK, crystal form 1), 24GD (apo-*Rp*HpsK, crystal form 2), 24GE (*Rp*HpsK•*S*-DHPS), 24GF (*Rp*HpsK•*R*-DHPS), 24GG (apo-*Bw*HpsK), and 24GH (*Bw*HpsK•*S*-DHPS)).

Supplementary information (SI): Fig. S1-S13, Tables S1-S7, experimental details, supplementary references (PDF). Supplementary Data files 1-3 contain proteomics data and sequence similarity network sequences (Excel).

## Acknowledgements

This work was supported by the Australian Research Council (ARC) through grants DP210100233, DP240100126 and DP250100819 (to S.J.W.) and Australian National Health and Medical Research Council Ideas grant 2018980 (to N.E.S.). M. L. is a recipient of Kaye Merlin Brutton Bequest Funding (University of Melbourne). A.W.E.S was supported by the Commonwealth through an Australian Government Research Training Program Scholarship. We thank Andreas Marquardt and Dr Laura Burchill for technical assistance. Aspects of this research was undertaken using the MX2 beamline at the Australian Synchrotron, part of ANSTO, and made use of the Australian Cancer Research Foundation (ACRF) detector. We thank the Australian Synchrotron beamline staff for their professional support. We acknowledge the use of the Melbourne Mass Spectrometry and Proteomics Facility, and the Melbourne Protein Characterisation Platform at the University of Melbourne.

## References

1 M. A. Moran and B. P. Durham, *Nat. Rev. Microbiol.*, 2019, **17**, 665-678.
2 K. B. Ksionzek, O. J. Lechtenfeld, S. L. McCallister, P. Schmitt-Kopplin, J. K. Geuer, W. Geibert and B. P. Koch, *Science*, 2016, **354**, 456-459.
3 E. Celik, M. Maczka, N. Bergen, T. Brinkhoff, S. Schulz and J. S. Dickschat, *Org. Biomol. Chem.*, 2017, **15**, 2919-2922.

View Article Online
DOI: 10.1039/D6SC02372J



4 B. Frommeyer, A. W. Fiedler, S. R. Oehler, B. T. Hanson, A. Loy, P. Franchini, D. Spiteller and D. Schleheck, *iScience*, 2020, **23**, 101510.
5 B. T. Hanson, D. K. Kits, J. Löffler, A. G. Burrichter, A. Fiedler, K. Denger, B. Frommeyer, C. W. Herbold, T. Rattei, N. Karcher, N. Segata, D. Schleheck and A. Loy, *ISME J.*, 2021, **15**, 2779–2791.
6 B. P. Durham, S. Sharma, H. Luo, C. B. Smith, S. A. Amin, S. J. Bender, S. P. Dearth, B. A. Van Mooy, S. R. Campagna, E. B. Kujawinski, E. V. Armbrust and M. A. Moran, *Proc. Natl. Acad. Sci. USA*, 2015, **112**, 453-457.
7 X. Chen, L. Liu, X. Gao, X. Dai, Y. Han, Q. Chen and K. Tang, *Environ. Int.*, 2021, **157**, 106829.
8 L. Liu, X. Gao, C. Dong, H. Wang, X. Chen, X. Ma, S. Liu, Q. Chen, D. Lin, N. Jiao and K. Tang, *ISME J.*, 2024, **18**, wrae084.
9 A. Burrichter, K. Denger, P. Franchini, T. Huhn, N. Müller, D. Spiteller and D. Schleheck, *Front. Microbiol.*, 2018, **9**, 2792.
10 J. Liu, Y. Wei, L. Lin, L. Teng, J. Yin, Q. Lu, J. Chen, Y. Zheng, Y. Li, R. Xu, W. Zhai, Y. Liu, Y. Liu, P. Cao, E. L. Ang, H. Zhao, Z. Yuchi and Y. Zhang, *Proc. Natl. Acad. Sci. USA*, 2020, **117**, 15599-15608.
11 B. P. Durham, A. K. Boysen, L. T. Carlson, R. D. Groussman, K. R. Heal, K. R. Cain, R. L. Morales, S. N. Coesel, R. M. Morris, A. E. Ingalls and E. V. Armbrust, *Nat. Microbiol.*, 2019, **4**, 1706-1715.
12 E. D. Goddard-Borger and S. J. Williams, *Biochem. J.*, 2017, **474**, 827–849.
13 W. F. Busby, *Biochim. Biophys. Acta*, 1966, **121**, 160-161.
14 W. F. Busby and A. A. Benson, *Plant Cell Physiol.*, 1973, **14**, 1123-1132.
15 B. E. Clifton, U. Alcolombri, G. I. Uechi, C. J. Jackson and P. Laurino, *Nature*, 2024, **634**, 721-728.
16 L. Burchill, A. Kaur, A. Nastasovici, M. Lee and S. J. Williams, *Chem. Sci.*, 2024, **15**, 15757-15768.
17 J. Mayer, T. Huhn, M. Habeck, K. Denger, K. Hollemeyer and A. M. Cook, *Microbiology*, 2010, **156**, 1556-1564.
18 X. Ma, H. Wang, L. Liu, H. Dang and K. Tang, *Int. J. Biol. Macromol.*, 2025, **306**, 141806.
19 F. X. Ferrer-González, B. Widner, N. R. Holderman, J. Glushka, A. S. Edison, E. B. Kujawinski and M. A. Moran, *ISME J.*, 2021, **15**, 762-773.
20 A. J. D. Snow, L. Burchill, M. Sharma, G. J. Davies and S. J. Williams, *Chem. Soc. Rev.*, 2021, **50**, 13628–13645.
21 Y. Chen, D. Liu, R. Chu, Z. Li, Y. Zhang, K. Ma, L. Jiang, Q. Yang, F. Lu, Y. Zhang and Y. Tong, *Front. Microbiol.*, 2026, **17**, 1758990.
22 X. Ma, H. Wang, C. Dong, L. Liu, X. Qiu, X. Chen, Q. Chen, L. Wang, Y. Zhang, N. Jiao, S. J. Williams and K. Tang, *Nat. Commun.*, 2026, **17**, 209.
23 J. Liu, Y. Wei, K. Ma, J. An, X. Liu, Y. Liu, E. L. Ang, H. Zhao and Y. Zhang, *ACS Catal.*, 2021, **11**, 14740-14750.
24 J. Li, R. Epa, N. E. Scott, D. Skoneczny, M. Sharma, A. J. D. Snow, J. P. Lingford, E. D. Goddard-Borger, G. J. Davies, M. J. McConville and S. J. Williams, *Appl. Environ. Microbiol.*, 2020, **86**, e00750-00720.

View Article Online
DOI: 10.1039/D6SC02372J



25 A. Kaur, P. L. van der Peet, J. W. Mui, M. Herisse, S. Pidot and S. J. Williams, *Arch. Microbiol.*, 2022, **204**, 193.
26 A. K. Felux, D. Spiteller, J. Klebensberger and D. Schleheck, *Proc. Natl. Acad. Sci. USA*, 2015, **112**, E4298-4305.
27 L. Liu, X. Chen, J. Ye, X. Ma, Y. Han, Y. He and K. Tang, *ISME J.*, 2023, **17**, 393-405.
28 J. Krasenbrink, B. T. Hanson, A. S. Weiss, S. Borusak, T. S. Tanabe, M. Lang, G. Aichinger, B. Hausmann, D. Berry, A. Richter, D. Marko, M. Mussmann, D. Schleheck, B. Stecher and A. Loy, *Microbiome*, 2025, **13**, 184.
29 J. Krasenbrink, S.-C. Chen, T. S. Tanabe, H. Sarikeçe, P. Meurs, S. Borusak, R. Samrat, G. Guan, C. Priemer, J. Osvatic, J. Séneca, B. Hausmann, D. R. Speth, E. Selberherr, W. Wanek, D. Schleheck, M. Mussmann and A. Loy, *ISME J.*, 2026, **20**, wrag069.
30 K. Denger, M. Weiss, A. K. Felux, A. Schneider, C. Mayer, D. Spiteller, T. Huhn, A. M. Cook and D. Schleheck, *Nature*, 2014, **507**, 114-117.
31 Y. Liu, Y. Wei, Y. Zhou, E. L. Ang, H. Zhao and Y. Zhang, *Biochem. Biophys. Res. Commun.*, 2020, **533**, 1109-1114.
32 M. Sharma, N. Pudlo, M. A. Järvå, A. Kaur, A. John, L. Burchill, J. P. Lingford, R. Epa, P. Abayakoon, N. E. Scott, J. P. Turkenburg, G. J. Davies, E. C. Martens, E. D. Goddard-Borger and S. J. Williams, *J. Biol. Chem.*, 2025, **301**, 108320.
33 J. An, Y. Wei, J. Liu, E. Lui Ang, H. Zhao and Y. Zhang, *Chembiochem*, 2021, **22**, 2862-2866.
34 J. S. Davies, M. J. Currie, R. C. J. Dobson, C. R. Horne and R. A. North, *Trends Biochem. Sci.*, 2024, **49**, 134-144.
35 M. F. Peter, J. A. Ruland, P. Depping, N. Schneberger, E. Severi, J. Moecking, K. Gatterdam, S. Tindall, A. Durand, V. Heinz, J. P. Siebrasse, P. A. Koenig, M. Geyer, C. Ziegler, U. Kubitscheck, G. H. Thomas and G. Hagelueken, *Nat. Commun.*, 2022, **13**, 4471.
36 J. S. Davies, M. J. Currie, R. A. North, M. Scalise, J. D. Wright, J. M. Copping, D. M. Remus, A. Gulati, D. R. Morado, S. A. Jamieson, M. C. Newton-Vesty, G. S. Abeysekera, S. Ramaswamy, R. Friemann, S. Wakatsuki, J. R. Allison, C. Indiveri, D. Drew, P. D. Mace and R. C. J. Dobson, *Nat. Commun.*, 2023, **14**, 1120.
37 M. C. Newton-Vesty, M. Scalise, S. A. Jamieson, M. J. Currie, H. G. Brown, S. Valimehr, Z. D. Tillett, K. R. Hall, S. Quan, J. R. Allison, A. E. Whitten, S. Panjikar, C. Indiveri, E. Hanssen, P. D. Mace, R. A. North, R. C. J. Dobson and J. S. Davies, *Structure*, 2026, **34**, 133-144.e135.
38 W. F. Schroer, H. E. Kepner, M. Uchimiya, C. Mejia, L. T. Rodriguez, C. R. Reisch and M. A. Moran, *ISME Commun.*, 2023, **3**, 37.
39 K. Denger, T. H. Smits and A. M. Cook, *Biochem. J.*, 2006, **394**, 657-664.
40 C. Dahl, B. Franz, D. Hensen, A. Kesselheim and R. Zigann, *Microbiology*, 2013, **159**, 2626-2638.
41 S. Boughanemi, P. Infossi, M. T. Giudici-Orticoni, B. Schoepp-Cothenet and M. Guiral, *Biochim. Biophys. Acta Bioenerg.*, 2020, **1861**, 148279.
42 K. Denger, S. Lehmann and A. M. Cook, *Microbiology*, 2011, **157**, 2983-2991.
43 A. Velazquez-Campoy and E. Freire, *Nat. Protoc.*, 2006, **1**, 186-191.
44 S. Sabrialabed, J. G. Yang, E. Yariv, N. Ben-Tal and O. Lewinson, *J. Biol. Chem.*, 2020, **295**, 5245-5256.
45 P. T. Nguyen, J. Y. Lai, J. T. Kaiser and D. C. Rees, *Protein Sci.*, 2019, **28**, 1750-1757.
46 L. T. Rosa, S. R. Dix, J. B. Rafferty and D. J. Kelly, *J. Mol. Biol.*, 2019, **431**, 351-367.

View Article Online
DOI: 10.1039/D6SC02372J

47 H. Laue, M. Friedrich, J. Ruff and A. M. Cook, *J. Bacteriol.*, 2001, **183**, 1727-1733.
48 A. A. Santos, S. S. Venceslau, F. Grein, W. D. Leavitt, C. Dahl, D. T. Johnston and I. A. C. Pereira, *Science*, 2015, **350**, 1541-1545.
49 A. C. C. Barbosa, S. S. Venceslau and I. A. C. Pereira, *Proc. Natl. Acad. Sci. USA*, 2024, **121**, e2313650121.
50 R. Zallot, N. Oberg and J. A. Gerlt, *Biochemistry*, 2019, **58**, 4169-4182.
51 J. A. Gerlt, J. T. Bouvier, D. B. Davidson, H. J. Imker, B. Sadkhin, D. R. Slater and K. L. Whalen, *Biochim. Biophys. Acta*, 2015, **1854**, 1019-1037.
52 N. Oberg, R. Zallot and J. A. Gerlt, *J. Mol. Biol.*, 2023, **435**, 168018.
53 M. W. Vetting, N. Al-Obaidi, S. Zhao, B. San Francisco, J. Kim, D. J. Wichelecki, J. T. Bouvier, J. O. Solbiati, H. Vu, X. Zhang, D. A. Rodionov, J. D. Love, B. S. Hillerich, R. D. Seidel, R. J. Quinn, A. L. Osterman, J. E. Cronan, M. P. Jacobson, J. A. Gerlt and S. C. Almo, *Biochemistry*, 2015, **54**, 909-931.
54 M. Xing, Y. Wei, Y. Zhou, J. Zhang, L. Lin, Y. Hu, G. Hua, A. N. Nanjaraj Urs, D. Liu, F. Wang, C. Guo, Y. Tong, M. Li, Y. Liu, E. L. Ang, H. Zhao, Z. Yuchi and Y. Zhang, *Nat. Commun.*, 2019, **10**, 1609.
55 M. C. Newton-Vesty, M. J. Currie, J. S. Davies, S. Panjikar, A. Sethi, A. E. Whitten, Z. D. Tillett, D. M. Wood, J. D. Wright, M. J. Love, T. M. Allison, S. A. Jamieson, P. D. Mace, R. A. North and R. C. J. Dobson, *Biochem. J.*, 2024, **481**, 1901-1920.
56 C. D. Dawson, S. M. Irwin, L. R. F. Backman, C. Le, J. X. Wang, V. Vennelakanti, Z. Yang, H. J. Kulik, C. L. Drennan and E. P. Balskus, *Cell Chem. Biol.*, 2021, **28**, 1333-1346.e1337.
57 Y. Perez-Riverol, J. Bai, C. Bandla, D. García-Seisdedos, S. Hewapathirana, S. Kamatchinathan, D. J. Kundu, A. Prakash, A. Frericks-Zipper, M. Eisenacher, M. Walzer, S. Wang, A. Brazma and J. A. Vizcaíno, *Nucleic Acids Res.*, 2022, **50**, D543-D552.

View Article Online
DOI: 10.1039/D6SC02372J



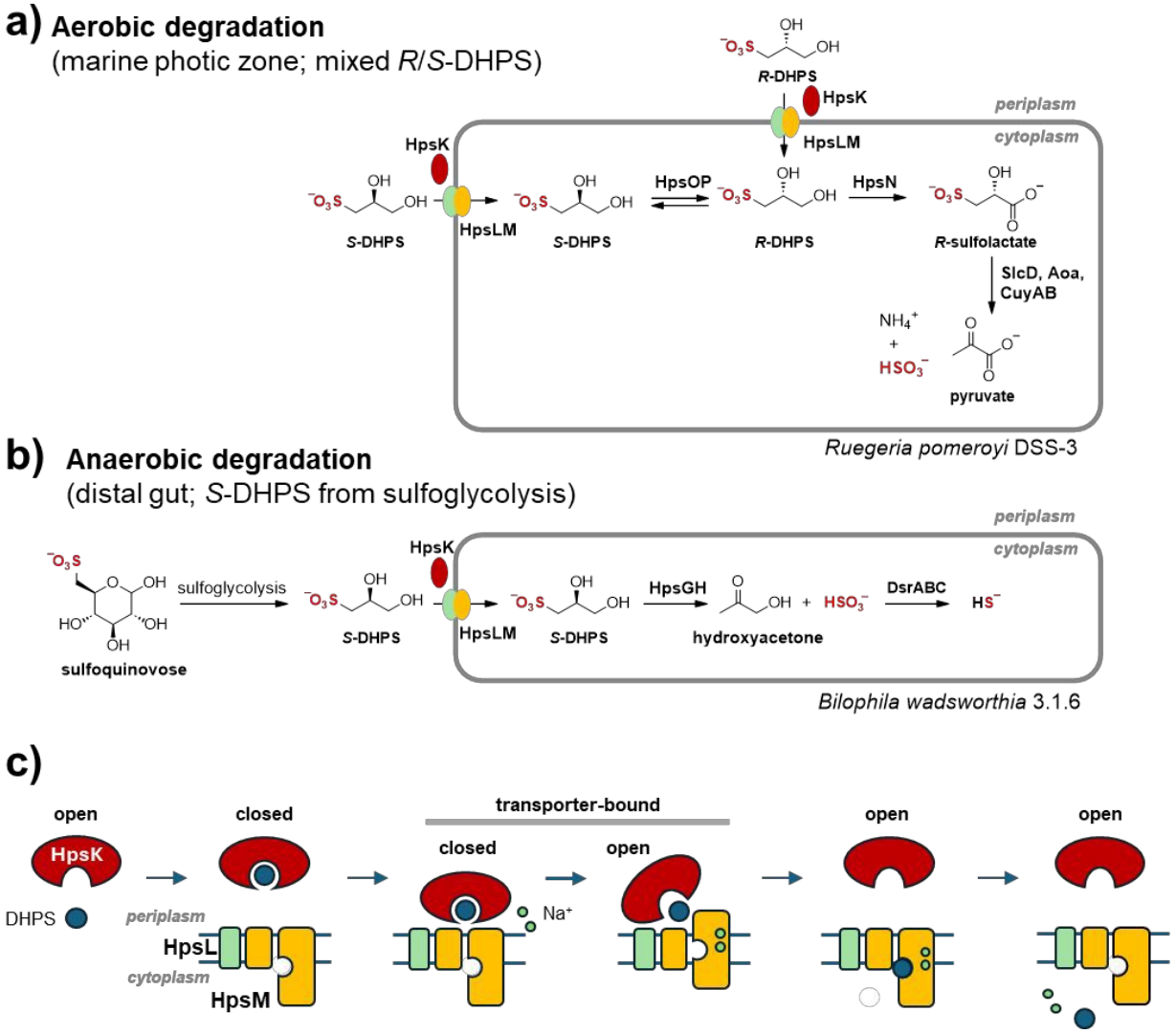


**Figure 1** Ecological contexts for 2,3-dihydroxypropanesulfonate (DHPS) import and catabolism. **a**) Aerobic DHPS utilisation in the marine bacterium *Ruegeria pomeroyi* DSS-3, where DHPS from dissolved organic matter is imported by the TRAP transporter HpsKLM and metabolised via the HpsNOP–CuyAB pathway. **b**) Anaerobic DHPS respiration in *Bilophila wadsworthia* 3.1.6, in which *S*-DHPS derived from sulfoquinovose degradation is imported and cleaved by the glycyl radical enzyme system HpsGH. **c**) Overview of ligand import by a tripartite ATP-independent periplasmic (TRAP) transporter comprising the periplasmic solute-binding protein (HpsK) and the membrane components HpsL and HpsM.

View Article Online
DOI: 10.1039/D6SC02372J



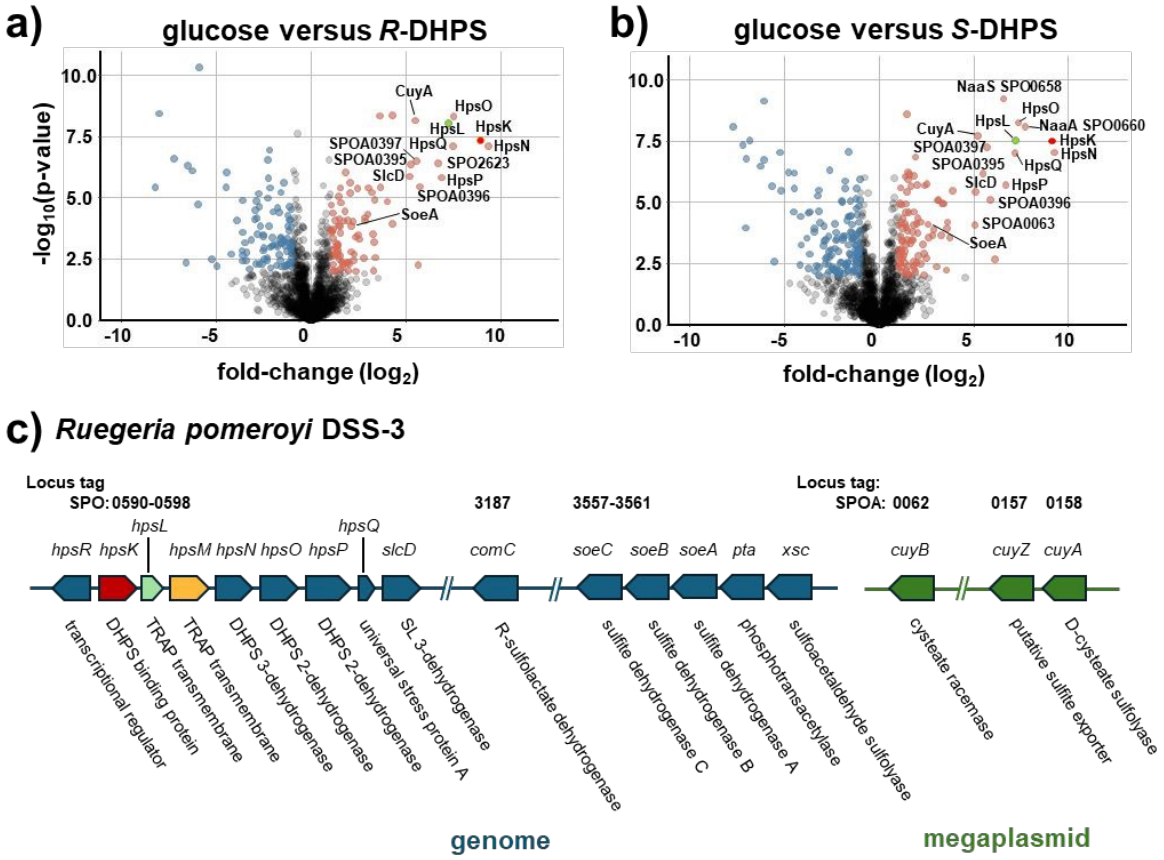


**Figure 2. Comparative proteomics of *Ruegeria pomeroyi* DSS-3 supports involvement of the TRAP transporter HpsKLM in DHPS utilisation.** (**a**) Volcano plot showing proteins significantly increased in abundance during growth on *R*- or *S*-DHPS relative to glucose. (**b**) Genomic loci encoding the HpsKLM TRAP transporter and associated enzymes implicated in DHPS import and downstream catabolism.

View Article Online
DOI: 10.1039/D6SC02372J



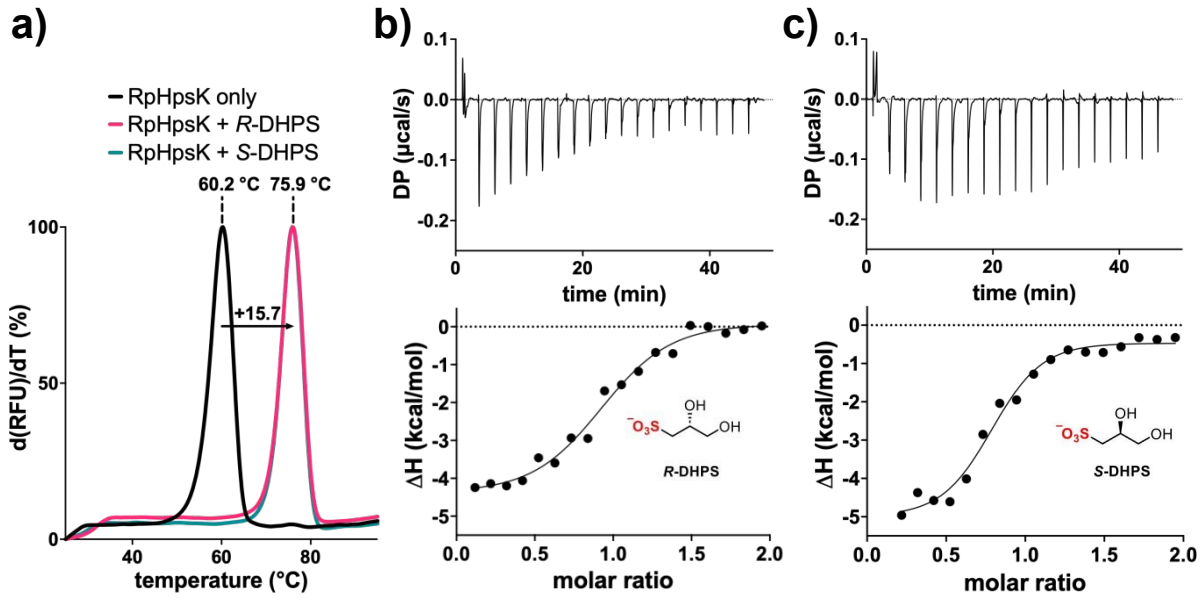


**Figure 3. *R. pomeroyi* HpsK binds *R*- and *S*-DHPS with low nanomolar affinity. a**) Nano-differential scanning fluorimetry (nanoDSF) thermograms showing change in melting temperature of *Rp*HpsK in the presence of 2 mM DHPS enantiomers. Isothermal titration calorimograms and binding isotherms of *Rp*HpsK titrated with (**b**) *R*-DHPS and (**c**) *S*-DHPS. Owing to the high affinity of *Rp*HpsK for DHPS, ITC experiments were performed under competitive displacement conditions in the presence of 200 µM hydroxypropanesulfonate (HPS), a weaker competing ligand.

View Article Online
DOI: 10.1039/D6SC02372J



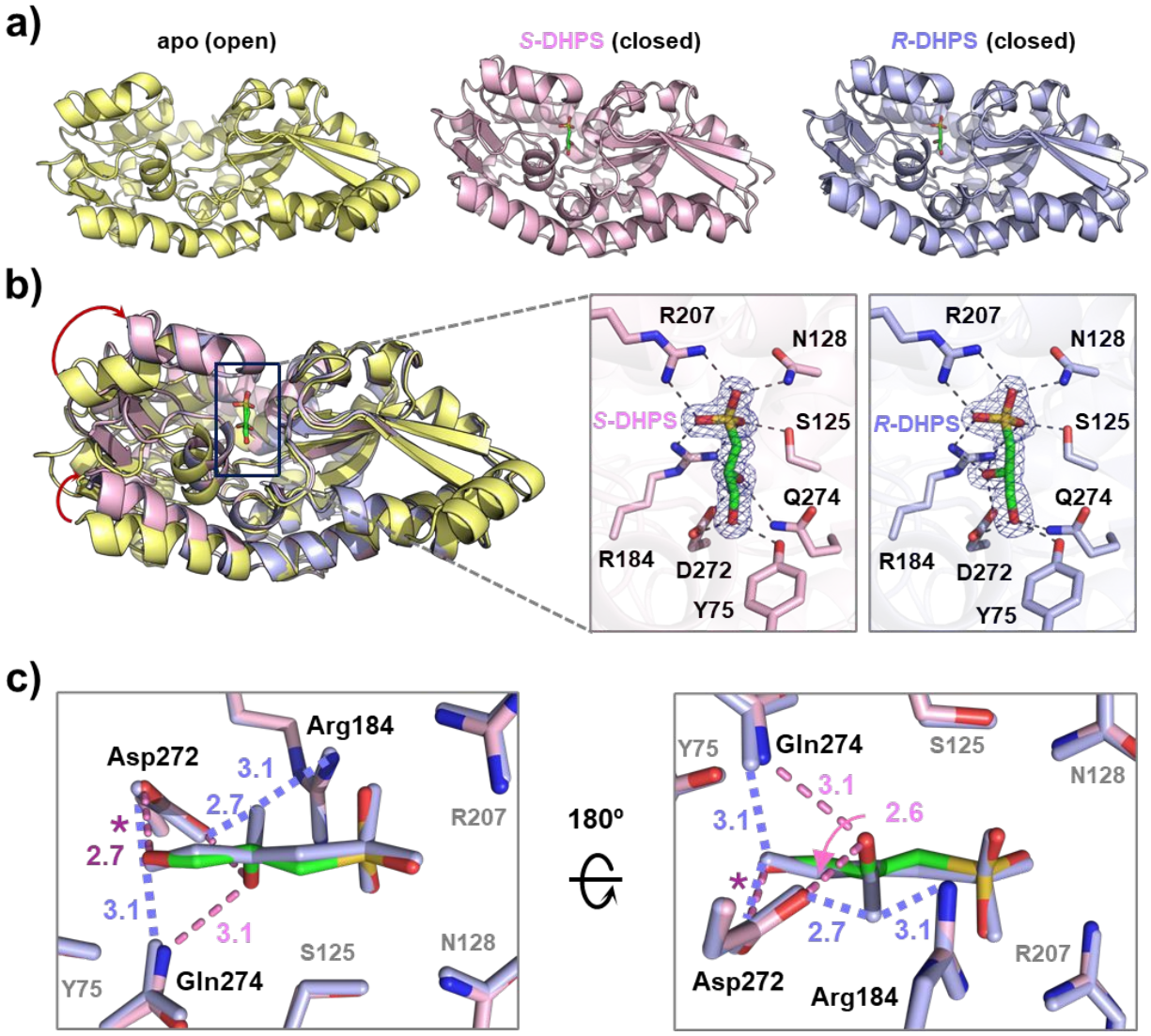


**Figure 4. Crystal structures of *R. pomeroyi* HpsK. a**) Overall structures of apo-HpsK (yellow), HpsK•*S*-DHPS (pink) and HpsK•*R*-DHPS (lavender). Ligand binding induces a closed conformation relative to the apo structure. **b**) Structural overlay of apo-HpsK, HpsK•*S*-DHPS (pink) and HpsK•*R*-DHPS (lavender) highlighting domain closure upon ligand binding. Right, close-up views of the DHPS binding sites showing side chains involved in substrate recognition. 2*F*o – *F*c electron density maps (blue mesh) are contoured at 1 σ. **c**) Overlay of HpsK•*S*-DHPS (pink) and HpsK•*R*-DHPS (lavender) showing minimal differences in the hydrogen-bonding network that coordinates DHPS. The conserved positioning of Asp272 enables dual recognition of both DHPS enantiomers. Hydrogen-bonding interactions specific to *S*-DHPS and *R*-DHPS are shown in pink and lavender dashes, respectively. The numbers next to the dashed lines are

View Article Online
DOI: 10.1039/D6SC02372J

hydrogen-bond distances in Å. The purple asterisk highlights overlaid hydrogen-bonds for the *R*- and *S*-DHPS complexes.



View Article Online
DOI: 10.1039/D6SC02372J



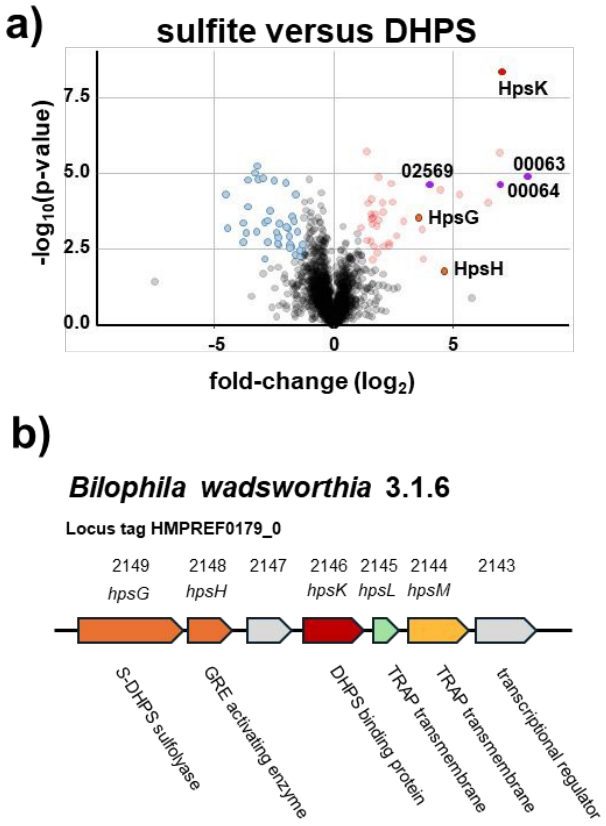


**Figure 5. Comparative proteomics of *Bilophila wadsworthia* 3.1.6 supports involvement of the TRAP transporter HpsKLM in DHPS utilisation**. **a**) Volcano plot showing proteins significantly increased in abundance during growth on rac-DHPS as terminal electron acceptor versus sulfite. **b**) Genomic loci encoding the HpsKLM TRAP transporter and associated enzymes implicated in DHPS import and catabolism. Purple dots indicate HMPREF0179_00063 and HMPREF0179_00064 (annotated as associated with TRAP transporters) and HMPREF0179_02569 (annotated as associated with an ABC transporter).

View Article Online
DOI: 10.1039/D6SC02372J



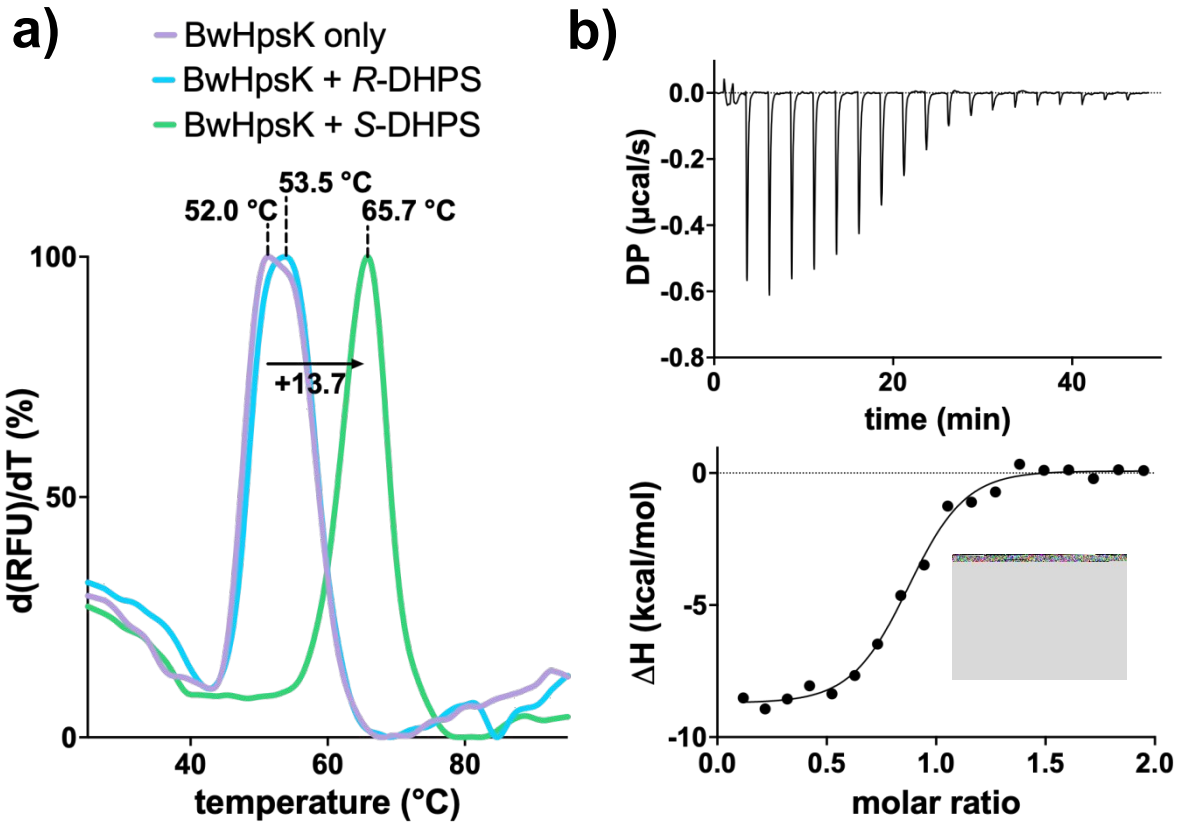


**Figure 6.** ***B. wadsworthia*** **HpsK selectively binds** ***S*****-DHPS. a**) Nano-differential scanning fluorimetry thermograms showing change in melting temperature of HpsK in the presence of 2 mM DHPS enantiomers. **b**) Isothermal titration calorimogram and binding isotherm of *Bw*HpsK titrated with *S*-DHPS.

View Article Online
DOI: 10.1039/D6SC02372J



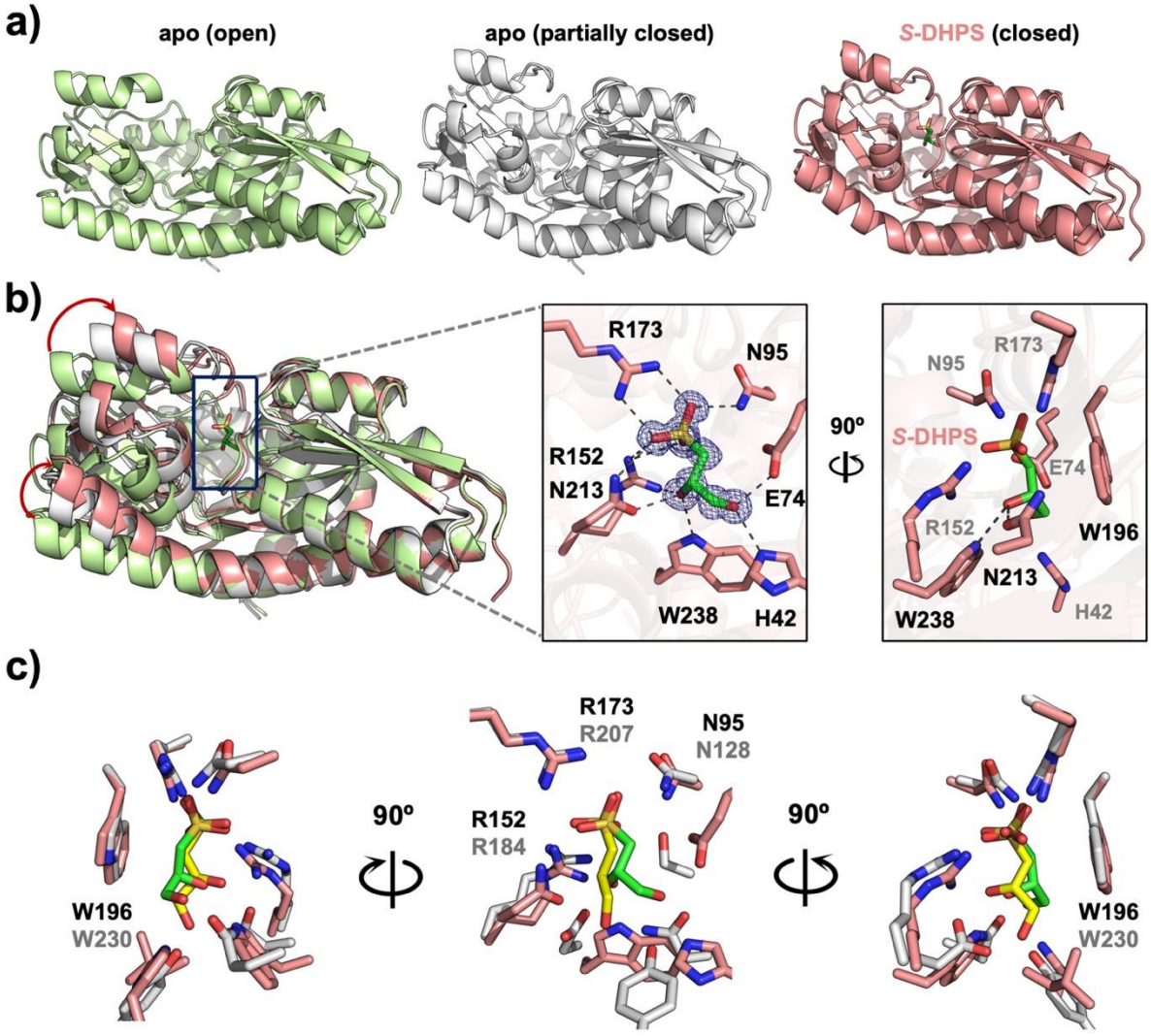


**Figure 7. Crystal structures of *B. wadsworthia* HpsK. a**) Overall structures of apo-*Bw*HpsK showing chain A in an open conformation (avocado green) and chain B in a partially closed conformation (grey), compared with the *Bw*HpsK•*S*-DHPS complex (salmon), which adopts a fully closed conformation. **b**) Structural overlay of apo-*Bw*HpsK and *Bw*HpsK•*S*-DHPS (salmon) highlighting ligand-induced domain closure. Right, close-up views of the *S*-DHPS binding site showing residues involved in substrate recognition. Residues implicated in *S*-DHPS selectivity form hydrogen bonds with Asn213 and Trp238 and a hydrophobic interaction with Trp196. 2*F*o – *F*c electron density maps (blue mesh) are contoured at 1 σ. **c**) Comparison of *S*-DHPS recognition in *Bw*HpsK•*S*-DHPS (protein carbon atoms in salmon, ligand carbons in green) and *Rp*HpsK•*S*-DHPS (protein carbon atoms in light grey; ligand carbons in yellow).

View Article Online
DOI: 10.1039/D6SC02372J



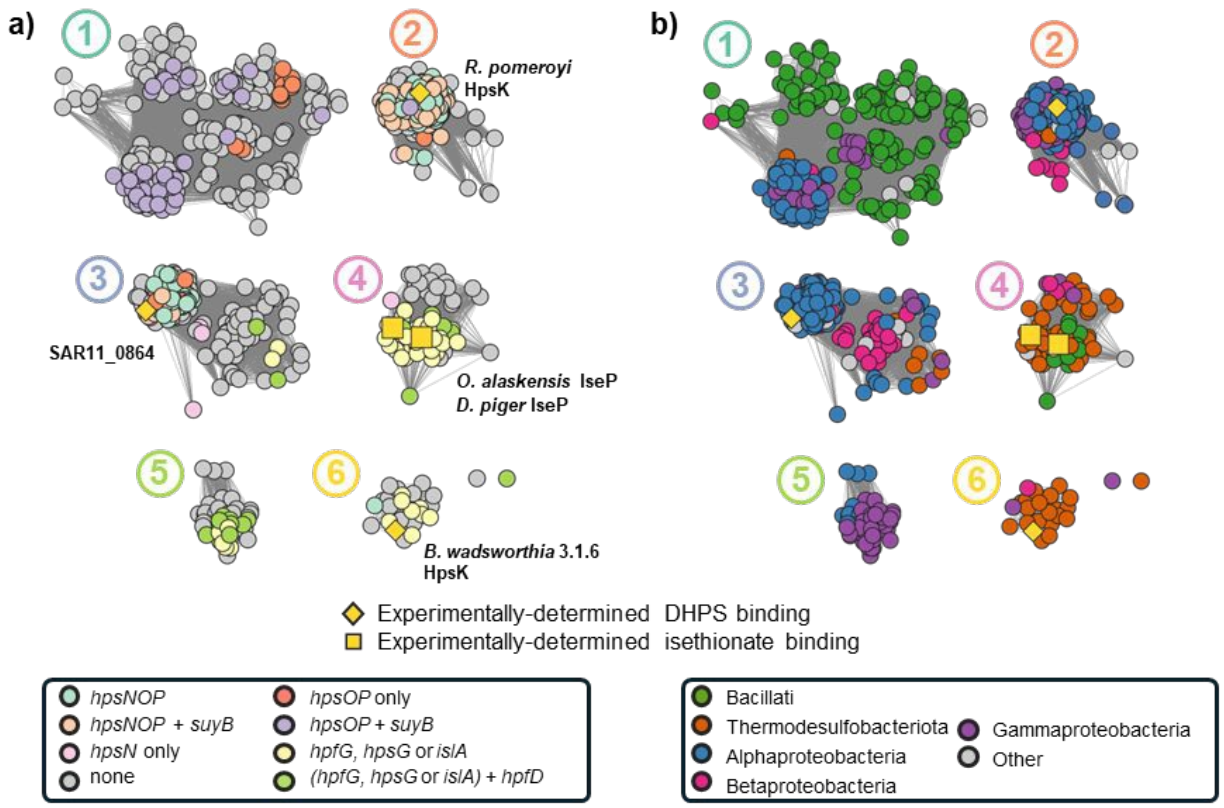


**Figure 8.** Sequence similarity network analysis of isethionate and DHPS binding HpsK homologues, and representative HpsK encoding gene clusters. a) Nodes colored for *hpsK* genome neighborhoods containing homologs encoding HpsNOP oxidative pathway variants and glycyl radical enzyme-linked HpsGH/HpfGH/IslAB pathways. b) Nodes colored for taxonomy of bacteria encoding HpsK homologs. SSNs are at alignment score of 80, corresponding to approximately 40% sequence identity.

View Article Online
DOI: 10.1039/D6SC02372J



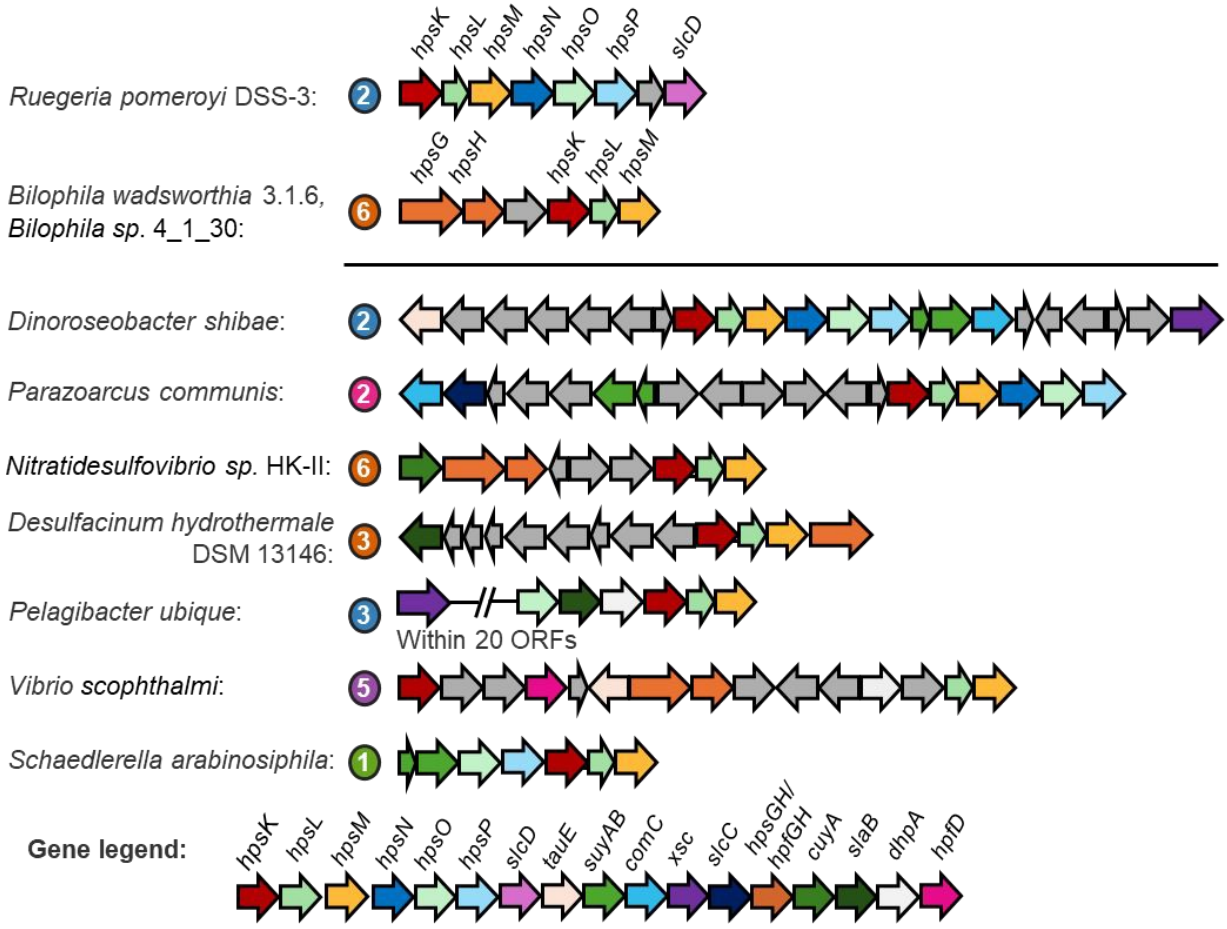


**Figure 9.** Genomic context of selected putative HpsK genes associated with sequence similarity network clusters 1, 2, 5 and 6, compared to *R. pomeroyi* and *Bilophila* sp. Representative genome diagrams for selected species spanning taxonomic groups and downstream DHPS metabolic pathways. Colored circles indicate cluster numbers and taxonomic groupings are consistent with SSN coloring in **Figure 8**.

View Article Online
DOI: 10.1039/D6SC02372J



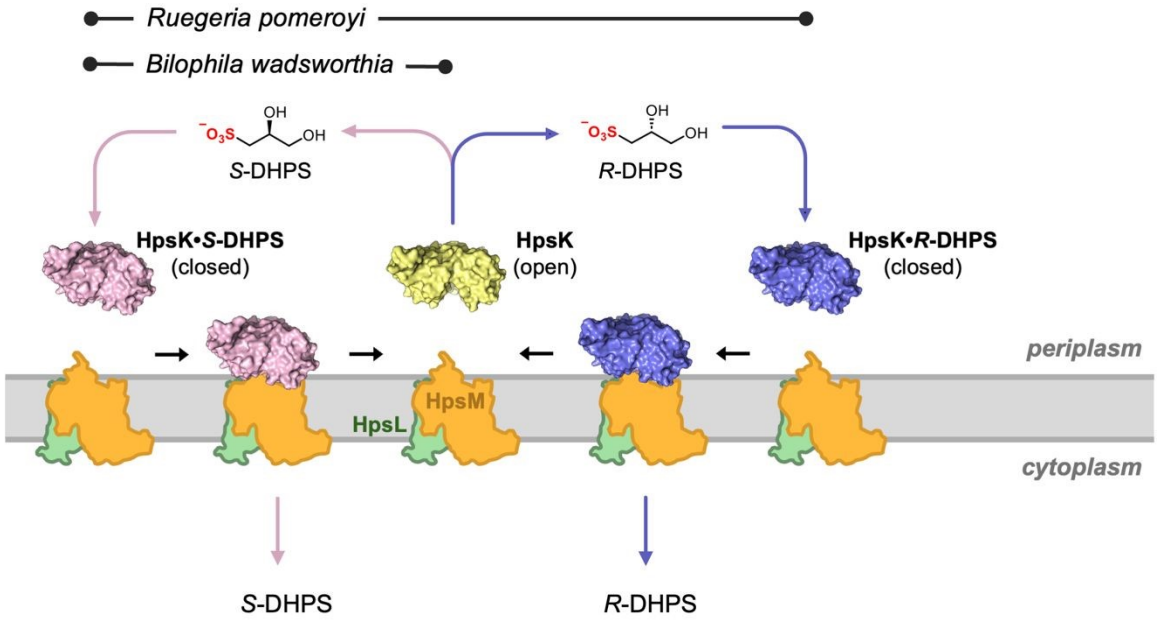


**Figure 10.** Overview of DHPS import in *R. pomeroyi* DSS-3 and *B. wadsworthia*.

## Data availability

View Article Online
DOI: 10.1039/D6SC02372J

The mass spectrometry proteomics data has been deposited in the Proteome Xchange Consortium via the PRIDE partner repository[42] with the data set identifier: PXD069364 (for the proteomics analysis of *Ruegeria pomeroyi* grown on DHPS) and PXD075985 (for the proteomics analysis of *Bilophila wadsworthia* grown on DHPS).

Data is accessible for the reviewer. With PXD069364 accessible with the Username: reviewer_pxd069364@ebi.ac.uk Password: 0neQwMDNCapv and PXD075985 accessible with the Username: & Password: eQqiVnyXzLBp

Structural data (atomic coordinates) of HpsK crystal structures have been deposited with the Protein Data Bank (PDB accession codes: 24GC (apo-*Rp*HpsK, crystal form 1), 24GD (apo-*Rp*HpsK, crystal form 2), 24GE (*Rp*HpsK•*S*-DHPS), 24GF (*Rp*HpsK•*R*-DHPS), 24GG (apo-*Bw*HpsK), and 24GH (*Bw*HpsK•*S*-DHPS)).

Supplementary information (SI): Fig. S1-S10, Tables S1-S5, experimental details, supplementary references (PDF). Table S6 containing sequence similarity network sequences (Excel).